

Geometric Adversarial Attacks and Defenses on 3D Point Clouds

Itai Lang
Tel Aviv University
itailang@mail.tau.ac.il

Uriel Kotlicki
Tel Aviv University
kotlicki@mail.tau.ac.il

Shai Avidan
Tel Aviv University
avidan@eng.tau.ac.il

Abstract

Deep neural networks are prone to adversarial examples that maliciously alter the network's outcome. Due to the increasing popularity of 3D sensors in safety-critical systems and the vast deployment of deep learning models for 3D point sets, there is a growing interest in adversarial attacks and defenses for such models. So far, the research has focused on the semantic level, namely, deep point cloud classifiers. However, point clouds are also widely used in a geometric-related form that includes encoding and reconstructing the geometry.

In this work, we explore adversarial examples at a geometric level. That is, a small change to a clean source point cloud leads, after passing through an autoencoder model, to a shape from a different target class. On the defense side, we show that remnants of the attack's target shape are still present at the reconstructed output after applying the defense to the adversarial input. Our code is publicly available¹.

1. Introduction

A point cloud is an important 3D data representation. It is lightweight in memory, simple in form, and very common as the output of a 3D sensor. In recent years, deep learning methods have been very successful in processing point clouds. Applications range from high-level tasks, such as classification [29, 30, 39], semantic segmentation [17, 35, 37], and object detection [28, 32, 43], to low-level tasks, such as down- and up-sampling [7, 18, 21, 44], denoising [13, 31], and reconstruction [1, 11, 42].

Despite their great success, neural networks are vulnerable to adversarial attacks. This topic has drawn much attention in the case of 2D images, where the main focus has been on the *semantic* level - adversarial examples that mislead image classifiers [3, 10, 27].

Very recently, semantic adversarial attacks have been extended to 3D point cloud classification [40, 48, 49] and

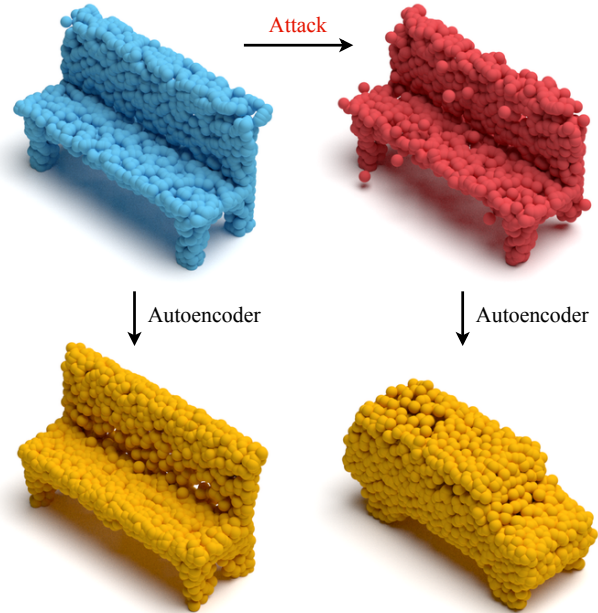


Figure 1. **A geometric adversarial attack.** Given a clean input point cloud (top left), our attack crafts an adversarial example (top right) that changes the *geometry* at the output of an *autoencoder* model (bottom row). In this example, it turns a *bench* into a *car*.

3D object detection in autonomous vehicles [2, 34, 36]. Nonetheless, a point cloud is a geometric entity. A natural question is whether an adversarial attack is possible at the *geometric* level. Meaning, can we make a small change to an input point cloud, feed it through an autoencoder network, and reconstruct a *geometrically different* output? This problem has not been studied before.

This paper proposes a novel framework for geometric adversarial attacks and defenses on 3D point clouds. We assume that a point cloud is to be processed by an autoencoder model. The encoder and decoder may be separate, for example, at a client unit and a server, respectively. Given a clean shape from a source shape class, our attack changes the reconstructed geometry to a point cloud from a semantically different target class.

¹https://github.com/itailang/geometric_adv

Two attack variants are explored: one is a gray-box attack that only has access to the encoder and operates on the latent space of the autoencoder; the other is a white-box attack that has access to both the encoder and decoder and operates on the output space. The first attack crafts an adversarial example that is encoded to a target latent vector. The second one minimizes the reconstruction error with respect to a desired output shape (see an example in Figure 1). In addition, we examine the transferability of our attacks to other autoencoder models.

We also suggest two types of defenses. One defense removes off-surface points, which are an artifact of our attacks. These 3D points are shifted by the attack out of the shape’s surface and seem to be “floating” around it. This defense is architecture-independent. The other defense drops points that are critical to the malicious reconstruction. It depends on the architecture of the autoencoder that we attack [1]. We use geometric metrics to measure the success of our attacks and defenses. Additionally, we evaluate the semantic interpretation of reconstructed adversarial and defended point sets.

Our experiments show that geometric attacks are feasible, in the sense that a small perturbation to a clean point set causes the autoencoder to output a different shape. The reconstructed target point cloud of the attack has a comparable and, in some cases, even better quality than the autoencoder’s reference reconstruction. It suggests that defense for mitigating the attack’s effect can only be carried out on the encoder side due to the high reconstruction performance of the adversarial examples.

Even on the encoder side, the attacks are not entirely defendable. Some features of the target shape survive the defense and appear in the reconstruction of the defended point set. Nevertheless, the defense recovers the semantics of the source class in most of the cases. To summarize, our key contributions are as follows:

- Novel adversarial attacks for point cloud reconstruction and evaluation of their transferability;
- Defense methods against the proposed attacks;
- Extensive geometric and semantic evaluation of the reconstructed adversarial and defended point clouds.

2. Related Work

Representation learning for point sets Nowadays, representation learning for 3D data is a prevalent research topic [20, 24, 25, 46]. A ubiquitous approach is to employ an encoder-decoder network architecture, typically referred to as an autoencoder (AE) [14]. The encoder encodes the essence of the input to a latent code-word. The decoder learns a transformation from the latent space back to the raw space to reconstruct the input. Another typical flavor is a variational autoencoder (VAE) [15], in which a statistical constraint is imposed on the learned latent space. In addition

to reconstruction, AE or VAE can be used for other applications, such as shape classification [42], morphing [11], editing [23, 26], analogies [1], and synthesis [5, 9], in an intuitive and elegant manner.

A variety of AEs have been proposed for point clouds. Achlioptas *et al.* [1] proposed an AE that operates directly on the 3D coordinates of the cloud. Its architecture, based on PointNet’s architecture [29], employs a per-point multi-layer perception (MLP) and a global max-pooling operation to obtain the latent representation of the input set. Then, several fully-connected layers regress the xyz coordinates back. A follow-up work enriched the encoder by aggregating information from neighboring points [42]. Researchers also suggested alternatives for the decoder, such as folding one or multiple 2D patches onto the surface of the 3D shape [11, 42]. In our work, we attack the widespread AE of Achlioptas *et al.* [1] and check the attack transferability to other common AEs, AtlasNet [11], and FoldingNet [42].

Adversarial attacks An adversarial attack creates an example that compromises a victim network’s behavior at the attacker’s will. Crafting an adversarial example is typically cast as an optimization problem, with an adversarial loss on the network’s output, along with a regularization term on the distortion of the input. Adversarial attacks have been thoroughly studied for 2D image classifiers [3, 10, 27, 33] and lately have been expanded to 3D point clouds [12, 40, 47].

Xiang *et al.* [40] pioneered adversarial attacks on the PointNet [29] classification model. They proposed two types of attacks: one that perturbs existing points, and the other that adds points to a clean example in a cluster or a pre-defined shape. Zheng *et al.* [48] and Zhang *et al.* [45] dropped points that influence the classifier’s label prediction in order to change it. Lee *et al.* [19] injected adversarial noise to the latent space of an AE instead of performing the attack at the point space. The decoded shape resembled the original one while serving as an adversarial example to a subsequent recognition model.

Previous works attacked classification networks for point sets to change their prediction. In contrast, in our work, we target an AE model and aim to alter the reconstructed geometry. Similar to our work, Kos *et al.* [16] studied adversarial examples for generative models for 2D images and proposed attacks that operate on the network’s latent or output space. We, however, use 3D data and geometric reasoning rather than pixel related metrics.

Defense methods Defense against adversarial attacks tries to mitigate the attack’s harmful effect. Several defense methods have been proposed for protecting 3D point cloud classifiers [6, 45, 50]. DUP-Net [50] removed out-of-surface points and increased the point cloud’s resolution to enable its correct classification. Liu *et al.* [22] used ad-

versarial examples during training for improving the robustness against such examples. Yang *et al.* [45] measured categorization stability under random perturbations to detect offensive inputs. Unlike this work, defense methods for point sets were studied for semantic point cloud recognition, not geometric reconstruction, as suggested in this paper.

In our work, we adopt an off-surface point filtering approach as a defense [22, 50]. Additionally, since the attacked AE [1] employs the PointNet architecture, it applies the critical points theorem [29]. Meaning, a subset of the input point cloud, denoted as critical points, determines its reconstructed output. While this notion has been used in the past for attacks [40, 45, 48], we leverage it here for defense.

3. Method

We attack an autoencoder (AE) trained on a collection of shapes from several semantic shape classes. We assume that a clean source point cloud is given for the attack. Our goal is to reconstruct a shape instance from a semantically *different* target shape class, with minimal distortion to the source *and* minimal reconstruction error of the target. The target class has various instances with the same semantic type, and we have the freedom to choose from them.

A naïve approach is to select the target instance at random. However, this approach is likely to fail since the AE is sensitive to the geometry at its input. A better approach is to choose a target shape that is geometrically similar to the source. Thus, for the given source, we select the nearest neighbor point clouds, in the Chamfer Distance sense (Equation 4), from the target shape class. See an illustration in Figure 2.

If only the encoder is known to the attacker, we treat it as a gray-box attack and work with the latent space of the AE. In a white-box setting, where both the encoder and decoder are accessible, we propose an output space attack that uses the reconstructed point cloud by the AE.

3.1. Attacks

A diagram of the proposed attacks is presented in Figure 3. A point cloud is defined as an unordered set of 3D coordinates $S \in \mathbb{R}^{n \times 3}$, where n is the number of points. Given a clean source shape S , we add an adversarial perturbation P to obtain an adversarial input Q :

$$Q = S + P. \tag{1}$$

Latent space attack We cast the attack as the following optimization problem. Given: $S \in \mathcal{S}$, a point cloud from a source shape class; \mathcal{T} , a semantically different target shape class; f_{Enc} , an encoder model. Find: $Q^* = S + P^*$, an adversarial example that is similar to S , and its encoding by f_{Enc} is close to a latent code of a point cloud instance T

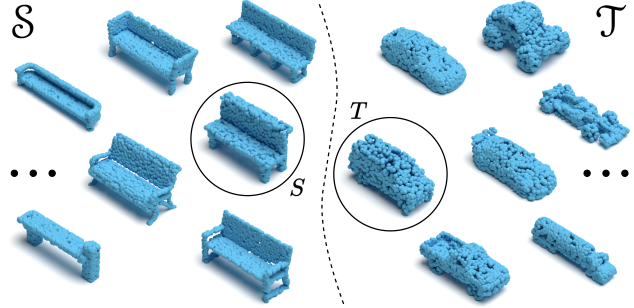


Figure 2. **Target selection.** For a given source point cloud in shape class \mathcal{S} , we select its geometric nearest neighbors, in the sense of Chamfer Distance, from a target shape class \mathcal{T} . These point clouds serve as candidates for the attack’s target. Here, we illustrate the geometrically closest target *car* instance T for a source *bench* shape S .

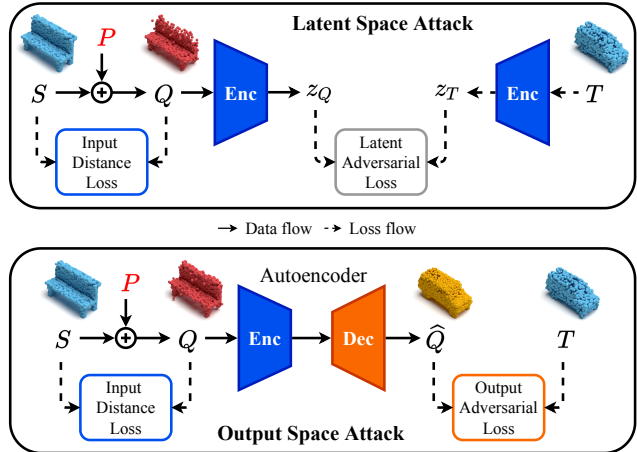


Figure 3. **The proposed attacks.** An adversarial perturbation P is added to a clean source point cloud S , resulting in a malicious input Q . In the latent space attack, P is optimized such that Q is encoded to a target latent vector z_T (top), while the output space attack aims to reconstruct a target point cloud T directly (bottom). In both cases, Q is required to resemble the source S .

from \mathcal{T} :

$$P^* = \underset{P}{\operatorname{argmin}} \mathcal{L}_{latent}(z_Q, z_T) + \lambda \mathcal{L}_{distance}(Q, S) \tag{2}$$

$$s.t. \quad z_Q = f_{Enc}(Q), \quad z_T = f_{Enc}(T), \quad T \in \mathcal{T},$$

where $S, Q, T \in \mathbb{R}^{n \times 3}$, $z_Q, z_T \in \mathbb{R}^m$, $\mathcal{T} \neq \mathcal{S}$, and λ is a hyperparameter.

This attack’s motivation is that proximity in the latent space can result in proximity in the output point space on the decoder side [41, 42]. Due to the Euclidean properties of the latent space [1], we use Euclidean loss between the latent vectors:

$$\mathcal{L}_{latent}(z_Q, z_T) = \|z_Q - z_T\|_2. \tag{3}$$

To regularize the attack and maintain similarity between Q and S , we use Chamfer Distance, a popular similarity measure between point clouds [1, 8, 38, 40]. The Chamfer Distance between two point clouds X and Y is given by:

$$CD(X, Y) = \frac{1}{|X|} \sum_{x \in X} \min_{y \in Y} \|x - y\|_2^2 + \frac{1}{|Y|} \sum_{y \in Y} \min_{x \in X} \|y - x\|_2^2. \quad (4)$$

Thus, the loss for the source and adversarial clouds is:

$$\mathcal{L}_{distance}(Q, S) = CD(Q, S). \quad (5)$$

Output space attack In case the adversary has access to the entire AE model, we suggest to attack the model’s output. For that attack, the problem statement in Equation 2 is changed as follows:

$$P^* = \underset{P}{\operatorname{argmin}} \mathcal{L}_{output}(\widehat{Q}, T) + \lambda \mathcal{L}_{distance}(Q, S) \quad (6)$$

s.t. $\widehat{Q} = f_{AE}(Q), \quad T \in \mathcal{T},$

where f_{AE} is the AE model, \widehat{Q} is the reconstruction of Q by f_{AE} , $\mathcal{T} \neq \mathcal{S}$, and λ is a hyperparameter.

The distance loss $\mathcal{L}_{distance}$ is the same as in Equation 5. To obtain the desired target shape T , we use Chamfer Distance as the adversarial loss:

$$\mathcal{L}_{output}(\widehat{Q}, T) = CD(\widehat{Q}, T). \quad (7)$$

Adversarial metrics Our attacks’ focus is to change the geometry of the shape at the output of the AE network. Thus, we use geometric measures to evaluate the performance of the attacks.

For the output, we report the *target* reconstruction error $T-RE = CD(\widehat{Q}, T)$. Since the AE model has an inherent error, we are also interested in the relative attack performance. Thus, we use the target normalized reconstruction error [7, 18], defined as:

$$T-NRE = \frac{CD(\widehat{Q}, T)}{CD(\widehat{T}, T)}, \quad (8)$$

where $\widehat{T} = f_{AE}(T)$.

For the input, we measure the distortion of the source shape by $S-CD = CD(Q, S)$. In addition, we observed that one artifact of our attacks is off-surface points, denoted as OS , in the adversarial point cloud Q (see Figure 4 for visualization). These points are noticeable to a human observer, and thereby, we wish their number to be minimal. We define OS points as points in Q whose distance to the nearest neighbor in S is larger than a threshold:

$$OS = \{q \in Q \mid \min_{s \in S} \|q - s\|_2 > \gamma\}. \quad (9)$$

Our goal is to optimize the attacks to achieve *both* minimal input and output metrics.

In addition to the geometric measures, we evaluate the semantic interpretation of the attack. Meaning, we check whether the adversarial examples’ reconstruction can mislead a classifier to the target shape class or avoid the source’s class label.

Scoring an attack The attack must reconcile two contradictory demands. On the one hand, it requires the perturbation of the source shape to be small. On the other, the reconstruction of the adversarial example has to match a true different target shape.

To cope with this challenge, we select candidate target instances that are close geometrically to the source, as explained at the beginning of this section. Moreover, we optimize each source-target pair with several different values of λ . We define a score:

$$r = (CD^2(Q, S) + CD^2(\widehat{Q}, T))^{\frac{1}{2}}, \quad (10)$$

and choose for each source the target instance and λ value that yield a minimal score. This process assumes access for the source distortion and target reconstruction error and improves the attacks’ success in both of them.

3.2. Defenses

Our defenses operate on the encoder side, on the malicious input point cloud. They intend to deflect adversarial points from the input to cancel out the attack’s effect on the reconstructed output. We propose two types of defenses. One relies on nearest neighbor statistics in the point cloud to remove off-surface points. This defense does not depend on the attacked AE model. The second defense takes advantage of the victim AE’s architecture. It identifies critical points that cause the adversarial reconstruction and filters them out.

Off-surface point removal In a clean point set, a point typically has neighboring points in its vicinity, on the shape’s surface. In contrast, an adversarial input may have points out-of-surface, which change the AE’s output.

To detect off-surface points, we compute the average distance to the k nearest neighbors for each point $q \in Q$:

$$\bar{d}_q = \frac{1}{k} \sum_{i \in \mathcal{N}_k(q)} \|q - q_i\|_2, \quad (11)$$

where $\mathcal{N}_k(q)$ includes the indices of the k closest points to q in Q , excluding q . Then, we keep points with an average distance less than or equal to a threshold δ and obtain the defended point cloud:

$$Q_{surf}^{def} = \{q \in Q \mid \bar{d}_q \leq \delta\}. \quad (12)$$

Thus, points that do not have close neighbors are removed.

Critical points removal The adversarial perturbation shifts points to locations that cause the AE to output the desired target shape. We leverage the architecture of the victim AE, which is based on PointNet [29], and identify these points as the critical points that determine the latent vector of the AE. The critical points defense takes the complementary points, thus reducing the effect of the attack on the reconstructed set. We denote the resulting point cloud of this defense as Q_{comp}^{def} .

Defense metrics We evaluate defense metrics before and after the defense is applied to the adversarial point cloud. Since the defense’s goal is to mitigate the attack’s effect, we measure reconstruction errors with respect to the source point set. The errors are given by $S-NRE_{before} = CD(\hat{Q}, S)$ and $S-NRE_{after} = CD(\hat{Q}^{def}, S)$, where \hat{Q}^{def} is either $f_{AE}(Q_{surf}^{def})$ or $f_{AE}(Q_{comp}^{def})$.

Similar to the attack evaluation (Equation 8), we factor in the AE’s error and also report the source normalized reconstruction error:

$$S-NRE_{before} = \frac{CD(\hat{Q}, S)}{CD(\hat{S}, S)} \quad (13)$$

$$S-NRE_{after} = \frac{CD(\hat{Q}^{def}, S)}{CD(\hat{S}, S)}, \quad (14)$$

where $\hat{S} = f_{AE}(S)$.

4. Results

4.1. Experimental Setup

We evaluate our attacks and defenses on point sets of $n = 2048$ points, sampled from CAD models of the ShapeNet Core55 database [4]. The point sets are normalized to the unit cube. We set the OS threshold $\gamma = 0.05$, *i.e.*, 5% of the cube’s size. We use the 13 largest shape classes from the database, which have more than 1000 examples each. Every class is split into 85%/5%/10% for train/validation/test sets. We align the shapes such that their long horizontal axis coincides with the x -axis.

We attack the prevailing point cloud AE of Achlioptas *et al.* [1]. The model is trained on the train set with the authors’ recommended settings, and then its parameters are frozen. The source and target shapes for our attacks are all taken from the test set.

We select 25 point clouds at random from each shape class as sources for the attack. Each source attacks the other 12 shape classes. For each source, we take 5 point sets as candidates for the attack from the target class, run the attack, and select one target instance per source, as explained at the end of sub-section 3.1. In total, we obtain $25 \cdot 13 \cdot 12 = 3900$ source-target pairs, which are regarded as a *targeted* attack.

For each source instance, the best result over the target classes, in terms of lowest attack score (Equation 10), is regarded as an *untargeted* attack. In this attack, there are $25 \cdot 13 = 325$ pairs. For consistency, results are reported and visualized here for the targeted setting, unless mentioned otherwise. We provide additional results, for targeted and untargeted settings, in the supplemental material.

The attacks are implemented on an Nvidia Titan Xp GPU. We optimize them with an Adam optimizer, learning rate 0.01, momentum 0.9, and 500 gradient steps. Additional optimization parameters appear in the supplementary.

4.2. Attack Evaluation

We evaluate the attacks in three aspects: geometric performance, semantic interpretation, and transferability. The first includes the adversarial metrics, as explained in sub-section 3.1. In the second, we check whether a classifier labels the adversarial reconstructions as their intended target shape class or if the source class label is avoided. In the third, we check our attacks’ geometric measures with AEs other than the victim one.

Geometric performance Table 1 presents the adversarial metrics for latent and output attacks. The results in the table are averaged over the targeted and untargeted source-target pairs. Figure 4 shows visualizations. The targeted latent attack results in 30 OS points and adds 65% to the AE’s reconstruction error for the target shape. The output attack reduces the number of OS points to 23, which is only about 1% of the point set’s total number of points. The $T-NRE$ of this attack is less by 56% compared to the latent space attack and is higher than the AE’s reference error by only 9%. The output attack even surpasses the AE’s reconstruction quality for the target point cloud in the untargeted setting.

The advantage of the latent space attack is that it does not need to know the decoder part of the network, and it back-propagates fewer gradients, only through the encoder part. However, this is also its drawback. The attack is limited, as it aims to produce the target’s latent vector and is unfamiliar with the decoding process that follows.

On the other hand, the output space attack has to know the entire AE model and propagates gradients from its end. However, it optimizes the target reconstruction directly, at the output of the AE. Since the attack is optimized per source-target pair, it can better reconstruct the target with an adversarial input than when the target itself is the input. We conclude that this attack is successful in the geometric sense: a small perturbation to the source results in the desired output geometry.

Semantic interpretation The semantics of our attacks are evaluated as follows. We employ the victim AE to compute reconstructions for the train set used for its training (sub-section 4.1). Then, we train a PointNet [29] classifier

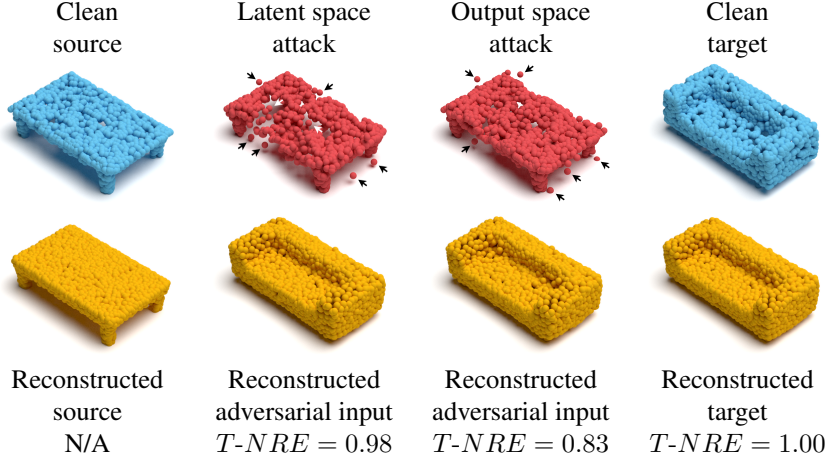


Figure 4. **Latent space vs. output space attack.** Top row: a clean source point cloud (*table*), adversarial examples of latent and output space attacks, and a clean target (*sofa*). Bottom row: corresponding reconstructions and their target normalized reconstruction error, $T-NRE$ (not applicable for the reconstructed source). We mark off-surface (*OS*) points for the attacks with arrows (part of them, to avoid clutter). The output space attack results in less distortion of the source shape and matches the AE’s reconstruction quality for a clean target.

Latent Space vs. Output Space Attack				
Attack Type	# <i>OS</i>	<i>S-CD</i>	<i>T-RE</i>	<i>T-NRE</i>
Latent (Tgt)	30	0.74	0.98	1.65
Output (Tgt)	23	0.44	0.61	1.09
Latent (unTgt)	17	0.32	0.42	1.07
Output (unTgt)	12	0.15	0.33	0.91

Table 1. **Geometric adversarial metrics.** We compare our latent and output space attacks in targeted (Tgt) and untargeted (unTgt) settings (see sub-section 4.1). The attacks are evaluated with the following metrics (in all cases, lower is better). *OS* (Equation 9) counts the number of off-surface points seen in an adversarial example. $S-CD = CD(Q, S)$ denotes Chamfer Distance between adversarial point cloud Q and clean *source* S , while $T-RE = CD(\hat{Q}, T)$ is the Chamfer Distance between reconstructed adversarial set \hat{Q} and clean *target* T . $S-CD$ and $T-RE$ are multiplied by a factor of 10^3 . $T-NRE$ (Equation 8) is the target normalized reconstruction error, relative to the AE’s inherent error. The output space attack is better than the latent space attack in terms of both source distortion and target reconstruction quality.

on these reconstructions. We utilize this classifier to check the classification accuracy for reconstructed adversarial inputs, where the ground truth label is the target shape class. We also measure whether the predicted label is different from that of the source shape. As a baseline, we measure the accuracy for reconstructed clean target point clouds selected for the attack. Table 2 summarizes the results.

We first notice that the baseline accuracy for clean targets is only 66%. This result sheds some light on the attack’s mechanism. The shape from a target class is selected at the boundary of the class, such that it is close *geometrically* to the source shape. These target instances confuse

Semantics of Reconstructed Point Clouds		
Input Type	Hit Target	Avoid Source
Clean target (w/o cls)	66.0%	92.6%
Latent attack (w/o cls)	48.9%	85.9%
Output attack (w/o cls)	52.1%	87.8%
Clean target (w/ cls)	100.0%	100.0%
Latent attack (w/ cls)	68.1%	90.8%
Output attack (w/ cls)	75.6%	94.0%

Table 2. **Semantic interpretation.** We show classification results for reconstructed shapes from *clean* targets, *latent* space attack, and *output* space attack. We measure the accuracy of predicting the target shape class label (Hit Target) or predicting a label other than the source class (Avoid Source). Targets are chosen from geometric nearest neighbor instances (top three rows) or only from neighbors with correct label prediction (bottom three rows). For all cases, higher is better. The 66% accuracy for clean targets in the first case is relatively low since the attack selects instances near the shape class boundary that are hard to recognize correctly. Including the semantic consideration for the target selection improves the results considerably. Please see the “Semantic interpretation” part in sub-section 4.2 for more details.

the classifier and result in relatively low accuracy. Still, the reconstructed targets avoid the source label for 92.6%.

The accuracy for the output space attack drops by just 13.9%, from 66% to 52.1%, and the source label is avoided 87.8% of the time. If we allow our attack to select only targets with correct semantic interpretation, the results are improved to 75.6% and 94%. Please see the supplementary for further discussion. To sum up, while our attack hits the target class label partially, in most cases, it misleads the classifier into a different shape class than that of the source.

Latent Space and Output Space Attacks Transfer		
Transfer Type	$T-RE$	$T-NRE$
Latent (MLP [1], different init)	3.04	5.16
Output (MLP [1], different init)	4.18	7.47
Latent (AtlasNet [11])	4.92	8.16
Output (AtlasNet [11])	7.19	12.59
Latent (FoldingNet [42])	7.62	12.87
Output (FoldingNet [42])	9.86	17.23

Table 3. **Geometric transfer metrics.** Adversarial examples are reconstructed by different AEs. See acronyms’ definition in Table 1. Init stands for initialization. $T-RE$ is multiplied by a factor of 10^3 . Lower is better. A transfer to a different AE results in high reconstruction error with respect to the attack’s *target* point cloud.

Transferability A typical test for an adversarial attack is whether it can be successfully transferred to a different model than the one it was designed for. We evaluate the transferability of our attacks by feeding their adversarial examples through different AEs. One AE has the same MLP architecture as the attacked AE [1] but different random weight initialization. The other AEs are the widely used AtlasNet [11] and FoldingNet [42].

We measure transferability with geometric metrics: the reconstruction error with respect to the *target* point cloud and its normalization by the victim AE’s original error (Equation 8). Results are reported in Table 3, and Figure 5 shows an example.

The examples of the latent space attack transfer better to other AEs than the output space attack examples. As the former is optimized through only the encoder part of the victim AE, it is less coupled with that AE and thus more transferable. Still, in both cases, the error is higher compared to that of the attacked AE (Table 1).

The error increase is since, in the transfer setting, the reconstructions are a mix of the source and target shapes, as presented in Figure 5. This behavior may be due to the typical nature of an AE: it mostly captures the essence of the input, rather than its peculiarities. We conclude that our attack is efficient when the model is known and degrades when it is not accessible to the adversary.

Failure cases Although the attack selects the nearest neighbors of the source from the target shape class, the geometry difference may still be large. In these cases, the attack causes high distortion to the source. We show examples of such cases in the supplementary.

Ablation study We examined candidate targets according to nearest neighbors in the latent space instead of the point space for the latent space attack. The attack performance was equivalent to that reported earlier in the paper (Table 1). Additional details about this ablative experiment and others are provided in the supplementary material.

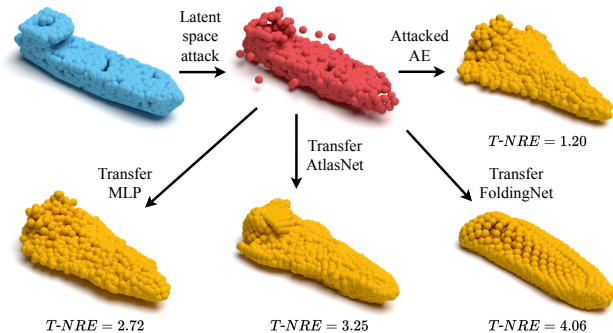


Figure 5. **Attack transfer.** Top row: a clean source (*watercraft*), an adversarial example (targeted to an *airplane*), and the reconstructed point cloud by the attacked AE [1]. In the bottom row, reconstructions by other AEs: an AE with the same architecture as the attacked one and different initialization (MLP), AtlasNet [11], and FoldingNet [42]. Here, the transfer to other AEs results in hybrids of airplane and watercraft shapes, and an increased $T-NRE$.

4.3. Defense Evaluation

Similar to the attack, the defense is evaluated geometrically (sub-section 3.2, "Defense metrics") and semantically (sub-section 4.2, "Semantic interpretation"). Unlike the attack, the metrics are computed with respect to the *source* rather than the *target* point set. In the semantic evaluation, we measure whether the defense returns the reconstruction of the defended input to the class label of the source.

Geometric performance The $S-RE$ and $S-NRE$ before and after defense, for off-surface and critical points removal, are detailed in Table 4. We report the defense’s effect on clean source point clouds and adversarial examples of latent and output space attacks. Figure 6 presents a visualization of defended inputs and their reconstructions.

Both defenses have a negligible influence on the reconstruction of a defended clean source. As it has on-surface points, the error remains the same after the off-surface defense. When critical points are removed, other points in their vicinity become critical, and the error is increased by only 2%. For an adversarial input, the defenses reduce the attack’s effect, as reflected by the lower $S-RE$ and $S-NRE$. However, the geometric error is still high.

As Figure 6 shows, the output after defense is indeed more similar to the source than the adversarial output. Yet, we notice a surprising behavior. Features from the target bleed to the reconstruction of the defended point set.

This phenomenon occurs since the attack not only moves points of the source to positions that cause the desired target reconstruction. It also perturbs points that prevent it. Thus, even after off-surface or critical points are removed, a residual effect of the attack is still present at the output. This result indicates the geometric effectiveness of our attack.

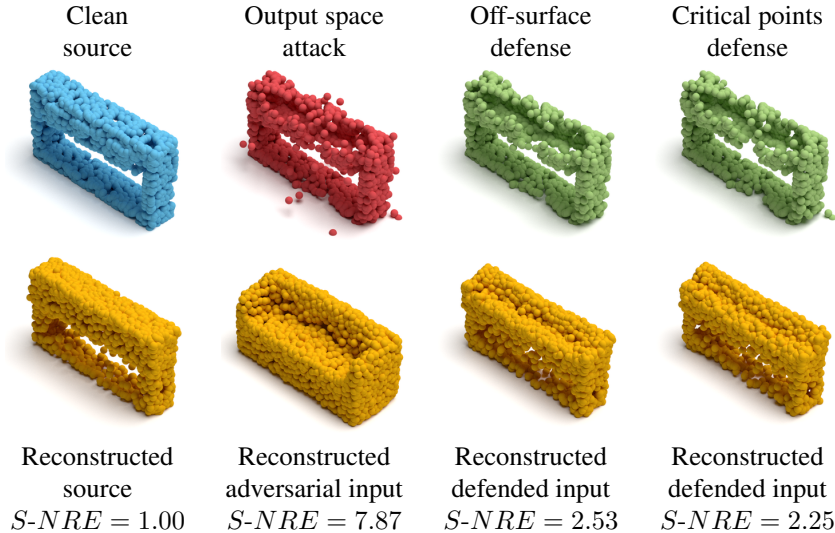


Figure 6. **Off-surface and critical points defenses.** Top row: a clean source point cloud (*table*), an adversarial example of the output space attack (targeted to a *sofa*), defended point cloud by the off-surface defense, and defended point cloud by the critical points defense. Bottom row: corresponding reconstructions and their source normalized reconstruction error, $S-NRE$, before defense (two results on the left) and after defense (two results on the right). While both defenses remove offensive points from the input, remnants of the attack’s target still appear in the output reconstruction. Here, instead of a flat surface, the top of the reconstructed table after defense resembles the sofa’s seat.

Before/After Off-Surface <i>or</i> Critical Points Defense			
Defense Type	$S-RE$ ↓	$S-NRE$ ↓	$S-RCA$ ↑
Surface (Src)	0.58/ 0.58	1.00/ 1.00	92.0%/ 92.0%
Critical (Src)	0.58/0.59	1.00/1.02	92.0%/91.4%
Surface (Lat)	8.27/2.50	21.10/4.90	14.1%/67.2%
Critical (Lat)	8.27/ 2.49	21.10/ 4.82	14.1%/ 68.3%
Surface (Out)	9.76/1.77	24.77/3.17	12.2%/76.6%
Critical (Out)	9.76/ 1.73	24.77/ 3.13	12.2%/ 77.7%

Table 4. **Geometric defense metrics and semantics.** Off-surface or critical points defense is applied to both latent (Lat) and output (Out) space attacks. For comparison, we also include defense results for clean source shapes (Src). $S-RE$, $S-NRE$, and $S-RCA$ stand for source reconstruction error, source normalized reconstruction error, and source reconstruction classification accuracy. The first is in geometric distance units, the second is relative to the baseline error of the attacked AE, and the third is the percentage of correctly classified instances as the *source* class label. $S-RE$ is multiplied by a factor of 10^3 . The arrow indicates whether lower or higher is better. The defenses reduce the reconstruction error with respect to the *source* point cloud and increase the classification accuracy.

Semantic interpretation For the defenses’ semantic evaluation, we use the same classifier utilized for the attack evaluation, where the ground truth label now is that of the *source* shape class. As reported in Table 4, the reference classification accuracy for reconstructed clean source point clouds used for the attack is 92%.

Before the defense, the accuracy of adversarial examples

is very low - less than 15%. However, applying the defense causes a substantial improvement. For instance, the critical points defense against the output space attack increases the accuracy to 77.7%. This result is only far by 14.3% from the reference accuracy of 92% for clean sources. We conclude that although the defense partially restores the source’s geometry, it succeeds in rescuing its semantic meaning.

5. Conclusions

In this paper, we presented geometric adversarial attacks and defenses on 3D point clouds. Our attacks aim to craft adversarial examples that change the reconstructed geometry by an autoencoder model. We suggested two attack variants: a gray-box attack that targets a latent vector, when there is access only to the encoder part of the network; and a white-box attack, in case the entire AE model is known, which optimizes a desired output shape directly, and yields better reconstruction performance than the first attack. Our defenses deflect off-surface or critical points from the adversarial examples to reduce their offensive effect.

Our study revealed an interesting duality between the proposed attacks and defenses. The attack is highly successful geometrically. Meaning, a small adversarial perturbation to the clean point set leads to a different output shape with low reconstruction error. However, it is interpreted semantically to the target class label for only half of the examples. In contrast, the defended point cloud’s reconstruction has a high geometric error with respect to the clean source. Still, the defense successfully restores its semantics.

References

- [1] Panos Achlioptas, Olga Diamanti, Ioannis Mitliagkas, and Leonidas J. Guibas. Learning Representations and Generative Models for 3D Point Clouds. In *Proceedings of the 35th International Conference on Machine Learning (ICML)*, pages 40–49, 2018. 1, 2, 3, 4, 5, 7, 17
- [2] Yulong Cao, Chaowei Xiao, Dawei Yang, Jing Fang, Ruigang Yang, Mingyan Liu, and Bo Li. Adversarial Objects Against LiDAR-Based Autonomous Driving Systems. *arXiv preprint arXiv:1907.05418*, 2019. 1
- [3] Nicholas Carlini and David Wagner. Towards Evaluating the Robustness of Neural Networks. *IEEE Symposium on Security and Privacy (SP)*, pages 39–57, 2017. 1, 2
- [4] Angel X. Chang, Thomas Funkhouser, Leonidas J. Guibas, Pat Hanrahan, Qixing Huang, Zimo Li, Silvio Savarese, Manolis Savva, Shuran Song, Hao Su, Jianxiong Xiao, Li Yi, and Fisher Yu. ShapeNet: An Information-Rich 3D Model Repository. *arXiv preprint arXiv:1512.03012*, 2015. 5, 12
- [5] Zhiqin Chen and Hao Zhang. Learning Implicit Fields for Generative Shape Modeling. In *Proceedings of the IEEE/CVF Conference on Computer Vision and Pattern Recognition (CVPR)*, pages 5939–5948, 2019. 2
- [6] Xiaoyi Dong, Dongdong Chen, Hang Zhou, Gang Hua, Weiming Zhang, and Nenghai Yu. Self-Robust 3D Point Recognition via Gather-Vector Guidance. In *Proceedings of the IEEE/CVF Conference on Computer Vision and Pattern Recognition (CVPR)*, pages 11516–11524, 2020. 2
- [7] Oren Dovrat, Itai Lang, and Shai Avidan. Learning to Sample. In *Proceedings of the IEEE/CVF Conference on Computer Vision and Pattern Recognition (CVPR)*, pages 2760–2769, 2019. 1, 4
- [8] Haoqiang Fan, Hao Su, and Leonidas Guibas. A Point Set Generation Network for 3D Object Reconstruction from a Single Image. In *Proceedings of the IEEE Conference on Computer Vision and Pattern Recognition (CVPR)*, pages 605–603, 2017. 4
- [9] Lin Gao, Jie Yang, Tong Wu, Yu-Jie Yuan, Hongbo Fu, Yu-Kun Lai, and Hao Zhang. SDM-NET: Deep Generative Network for Structured Deformable Mesh. *ACM Transactions on Graphics (TOG), Siggraph Asia 2019*, 38(6):Article 243, 2019. 2
- [10] Ian J. Goodfellow, Jonathon Shlens, and Christian Szegedy. Explaining and Harnessing Adversarial Examples. In *Proceedings of the International Conference on Learning Representations (ICLR)*, 2015. 1, 2
- [11] Thibault Groueix, Matthew Fisher, Vladimir G. Kim, Bryan C. Russell, and Mathieu Aubry. AtlasNet: A Papier-Mâché Approach to Learning 3D Surface Generation. In *Proceedings of the IEEE Conference on Computer Vision and Pattern Recognition (CVPR)*, pages 216–224, 2018. 1, 2, 7, 17
- [12] Abdullah Hamdi, Sara Rojas, Ali Thabet, and Bernard Ghanem. AdvPC: Transferable Adversarial Perturbations on 3D Point Clouds. In *Proceedings of the European Conference on Computer Vision (ECCV)*, pages 877–894, 2020. 2
- [13] Pedro Hermosilla, Tobias Ritschel, and Timo Ropinski. Total denoising: Unsupervised learning of 3d point cloud cleaning. In *Proceedings of the IEEE/CVF International Conference on Computer Vision (ICCV)*, pages 52–60, 2019. 1
- [14] Geoffrey E. Hinton and Ruslan R. Salakhutdinov. Reducing the Dimensionality of Data with Neural Networks. *Science*, 313:504–507, 2006. 2
- [15] Diederik P. Kingma and Max Welling. Auto-Encoding Variational Bayes. In *Proceedings of the International Conference on Learning Representations (ICLR)*, 2014. 2
- [16] Jernej Kos, Ian Fischer, and Dawn Song. Adversarial Examples for Generative Models. *IEEE Security and Privacy Workshops (SPW)*, pages 36–42, 2018. 2
- [17] Loic Landrieu and Martin Simonovsky. Large-scale Point Cloud Semantic Segmentation with Superpoint Graphs. In *Proceedings of the IEEE Conference on Computer Vision and Pattern Recognition (CVPR)*, pages 4558–4567, 2018. 1
- [18] Itai Lang, Asaf Manor, and Shai Avidan. SampleNet: Differentiable Point Cloud Sampling. In *Proceedings of the IEEE/CVF Conference on Computer Vision and Pattern Recognition (CVPR)*, pages 7578–7588, 2020. 1, 4
- [19] Kibok Lee, Zhuoyuan Chen, Xinchun Yan, Raquel Urtasun, and Ersin Yumer. ShapeAdv: Generating Shape-Aware Adversarial 3D Point Clouds. *arXiv preprint arXiv:2005.11626*, 2020. 2
- [20] Jiaxin Li, Ben M Chen, and Gim Hee Lee. SO-Net: Self-Organizing Network for Point Cloud Analysis. In *Proceedings of the IEEE Conference on Computer Vision and Pattern Recognition (CVPR)*, pages 9397–9406, 2018. 2
- [21] Ruihui Li, Xianzhi Li, Chi-Wing Fu, Daniel Cohen-Or, and Pheng-Ann Heng. PU-GAN: a Point Cloud Upsampling Adversarial Network. In *Proceedings of the IEEE/CVF International Conference on Computer Vision (ICCV)*, pages 7203–7212, 2019. 1
- [22] Daniel Liu, Ronald Yu, and Hao Su. Extending Adversarial Attacks and Defenses to Deep 3D Point Cloud Classifiers. In *Proceedings of the IEEE International Conference on Image Processing (ICIP)*, 2019. 2, 3
- [23] Éloi Mehr, Ariane Jourdan, Nicolas Thome, Matthieu Cord, and Vincent Guitteny. DiscoNet: Shapes Learning on Disconnected Manifolds for 3D Editing. In *Proceedings of the IEEE/CVF International Conference on Computer Vision (ICCV)*, pages 3474–3483, 2019. 2
- [24] Lars Mescheder, Michael Oechsle, Michael Niemeyer, Sebastian Nowozin, and Andreas Geiger. Occupancy Networks: Learning 3D Reconstruction in Function Space. In *Proceedings of the IEEE/CVF Conference on Computer Vision and Pattern Recognition (CVPR)*, pages 4460–4470, 2019. 2
- [25] Kaichun Mo, Paul Guerrero, Li Yi, Hao Su, Peter Wonka, Niloy Mitra, and Leonidas Guibas. StructureNet: Hierarchical Graph Networks for 3D Shape Generation. *ACM Transactions on Graphics (TOG), Siggraph Asia 2019*, 38(6):Article 242, 2019. 2
- [26] Kaichun Mo, Paul Guerrero, Li Yi, Hao Su, Peter Wonka, Niloy J. Mitra, and Leonidas Guibas. StructEdit: Learning Structural Shape Variations. In *Proceedings of the IEEE/CVF Conference on Computer Vision and Pattern Recognition (CVPR)*, pages 8859–8868, 2020. 2

- [27] Nicolas Papernot, Patrick McDaniel, Somesh Jha, Matt Fredrikson, Z. Berkay Celik, and Ananthram Swami. The Limitations of Deep Learning in Adversarial Settings. *IEEE European Symposium on Security and Privacy (EuroS&P)*, pages 372–387, 2016. [1](#), [2](#)
- [28] Charles R. Qi, Or Litany, Kaiming He, and Leonidas J. Guibas. Deep Hough Voting for 3D Object Detection in Point Clouds. *Proceedings of the International Conference on Computer Vision (ICCV)*, pages 9277–9286, 2019. [1](#)
- [29] Charles R. Qi, Hao Su, Kaichun Mo, and Leonidas J. Guibas. PointNet: Deep Learning on Point Sets for 3D Classification and Segmentation. In *Proceedings of the IEEE Conference on Computer Vision and Pattern Recognition (CVPR)*, pages 652–660, 2017. [1](#), [2](#), [3](#), [5](#), [18](#)
- [30] Charles R. Qi, Li Yi, Hao Su, and Leonidas J. Guibas. PointNet++: Deep Hierarchical Feature Learning on Point Sets in a Metric Space. In *Proceedings of Advances in Neural Information Processing Systems (NeurIPS)*, pages 5099–5108, 2017. [1](#)
- [31] Marie-Julie Rakotosaona, Vittorio La Barbera, Paul Guerrero, Niloy J. Mitra, and Maks Ovsjanikov. PointCleanNet: Learning to Denoise and Remove Outliers from Dense Point Clouds. *Computer Graphics Forum*, 39(1):185–203, 2020. [1](#)
- [32] Shaoshuai Shi, Xiaogang Wang, and Hongsheng Li. PointRCNN: 3D Object Proposal Generation and Detection From Point Cloud. In *The IEEE Conference on Computer Vision and Pattern Recognition (CVPR)*, pages 770–779, 2019. [1](#)
- [33] Jiawei Su, Danilo Vasconcellos Vargas, and Sakurai Kouichi. One Pixel Attack for Fooling Deep Neural Networks. *IEEE Transactions on Evolutionary Computation*, 23(5):828–841, 2019. [2](#)
- [34] Jiachen Sun, Yulong Cao, Qi Alfred Chen, and Z. Morley Mao. Towards Robust LiDAR-based Perception in Autonomous Driving: General Black-box Adversarial Sensor Attack and Countermeasures. In *Proceedings of the 29th USENIX Security Symposium*, 2020. [1](#)
- [35] Lyne P. Tchapmi, Christopher B. Choy, Iro Armeni, JunYoung Gwak, and Silvio Savarese. SEGCloud: Semantic Segmentation of 3D Point Clouds. In *Proceedings of the International Conference on 3D Vision (3DV)*, 2017. [1](#)
- [36] James Tu, Mengye Ren, Sivabalan Manivasagam, Ming Liang, Bin Yang, Richard Du, Frank Cheng, and Raquel Urtasun. Physically Realizable Adversarial Examples for LiDAR Object Detection. In *Proceedings of the IEEE/CVF Conference on Computer Vision and Pattern Recognition (CVPR)*, pages 13716–13725, 2020. [1](#)
- [37] Lei Wang, Yuchun Huang, Yaolin Hou, Shenman Zhang, and Jie Shan. Graph Attention Convolution for Point Cloud Semantic Segmentation. In *Proceedings of the IEEE/CVF Conference on Computer Vision and Pattern Recognition (CVPR)*, pages 10296–10305, 2019. [1](#)
- [38] Xiaogang Wang, Marcelo H. Ang Jr. , and Gim Hee Lee. Cascaded refinement network for point cloud completion. In *IEEE/CVF Conference on Computer Vision and Pattern Recognition (CVPR)*, pages 790–799, 2020. [4](#)
- [39] Yue Wang, Yongbin Sun, Ziwei Liu, Sanjay E. Sarma, Michael M. Bronstein, and Justin M. Solomon. Dynamic Graph CNN for Learning on Point Clouds. *ACM Transactions on Graphics (TOG)*, 2019. [1](#)
- [40] Chong Xiang, Charles R. Qi, and Bo Li. Generating 3D Adversarial Point Clouds. In *Proceedings of the IEEE/CVF Conference on Computer Vision and Pattern Recognition (CVPR)*, pages 9136–9144, 2019. [1](#), [2](#), [3](#), [4](#)
- [41] Guandao Yang, Xun Huang, Zekun Hao, Ming-Yu Liu, Serge Belongie, and Bharath Hariharan. PointFlow: 3D Point Cloud Generation With Continuous Normalizing Flows. In *Proceedings of the IEEE/CVF International Conference on Computer Vision (ICCV)*, pages 4541–4550, 2019. [3](#)
- [42] Yaoqing Yang, Chen Feng, Yiru Shen, and Dong Tian. FoldingNet: Point Cloud Auto-encoder via Deep Grid Deformation. In *Proceedings of the IEEE Conference on Computer Vision and Pattern Recognition (CVPR)*, pages 206–215, 2018. [1](#), [2](#), [3](#), [7](#), [17](#), [18](#)
- [43] Zetong Yang, Yanan Sun, Shu Liu, and Jiaya Jia. 3DSSD: Point-Based 3D Single Stage Object Detector. In *Proceedings of the IEEE/CVF Conference on Computer Vision and Pattern Recognition (CVPR)*, pages 11040–11048, 2020. [1](#)
- [44] Lequan Yu, Xianzhi Li, Chi-Wing Fu, Daniel Cohen-Or, and Pheng Ann Heng. PU-Net: Point Cloud Upsampling Network. In *Proceedings of the IEEE Conference on Computer Vision and Pattern Recognition (CVPR)*, pages 2790–2799, 2018. [1](#)
- [45] Qiang Zhang, Jiancheng Yang, Rongyao Fang, Bingbing Ni, Jinxian Liu, and Tian Qi. Adversarial Attack and Defense on Point Sets. *arXiv preprint arXiv:1902.10899*, 2019. [2](#), [3](#)
- [46] Yongheng Zhao, Tolga Birdal, Haowen Deng, and Federico Tombari. 3D Point Capsule Networks. In *Proceedings of the IEEE/CVF Conference on Computer Vision and Pattern Recognition (CVPR)*, pages 1009–1018, 2019. [2](#)
- [47] Yue Zhao, Yuwei Wu, Caihua Chen, and Andrew Lim. On Isometry Robustness of Deep 3D Point Cloud Models Under Adversarial Attacks. In *Proceedings of the IEEE/CVF Conference on Computer Vision and Pattern Recognition (CVPR)*, pages 1201–1210, 2020. [2](#)
- [48] Tianhang Zheng, Changyou Chen, Junsong Yuan, Bo Li, and Kui Ren. PointCloud Saliency Maps. In *Proceedings of the IEEE/CVF International Conference on Computer Vision (ICCV)*, pages 1961–1970, 2019. [1](#), [2](#), [3](#)
- [49] Hang Zhou, Dongdong Chen, Jing Liao, Kejiang Chen, Xiaoyi Dong, Kunlin Liu, Weiming Zhang, Gang Hua, and Nenghai Yu. LG-GAN: Label Guided Adversarial Network for Flexible Targeted Attack of Point Cloud Based Deep Networks. In *Proceedings of the IEEE/CVF Conference on Computer Vision and Pattern Recognition (CVPR)*, pages 10356–10365, 2020. [1](#)
- [50] Hang Zhou, Kejiang Chen, Weiming Zhang, Han Fang, Wenbo Zhou, and Nenghai Yu. DUP-Net: Denoiser and Upsampler Network for 3D Adversarial Point Clouds Defense. In *Proceedings of the IEEE/CVF International Conference on Computer Vision (ICCV)*, pages 1961–1970, 2019. [2](#), [3](#)

Supplementary Material

In the following sections, we provide additional information regarding our geometric attacks and defenses. Sections A and B provide more attack and defense results, respectively. The results are for the targeted setting, unless mentioned otherwise. An extensive ablation study is presented in Section C. Finally, in Section D, we detail experimental settings, including network architecture and optimization parameters for the victim autoencoder (AE), AEs for transfer, and classifier for semantic evaluation. Optimization timings are reported for an Nvidia Titan Xp GPU.

A. Additional Attack Results

A.1. Evolution of the Attack

We simulate our attack’s evolution by interpolating between a clean point set S and a corresponding adversarial example Q . Specifically, we compute:

$$U = (1 - \alpha)S + \alpha Q, \quad (15)$$

and:

$$\hat{U} = f_{AE}(U), \quad (16)$$

where $\alpha \in [0, 1]$ is an interpolation factor, and f_{AE} is the victim AE model. The process is shown in Figure 14, for the output space attack example in Figure 1 in the paper.

The attack starts by exploring points to perturb (first row in Figure 14). Then, it realizes that some points are not required for causing the target output. Thus, it shifts them towards the surface of the source shape to comply with the input distance loss (Equation 5) and continues to move the necessary points to satisfy the output adversarial loss (Equation 7). This process can be seen in the second and third rows of the figure. It implies that the attack converges to an adversarial example that maintains similarity to the source point cloud while achieving the desired target reconstruction.

A.2. Untargeted Attack Distribution

To gain more insight into the relations between shape classes, we analyze the statistics of the untargeted output space attack (sub-section 4.1). We compute the distribution over the selected target classes for the adversarial point clouds from each source class. Figure 7 presents the results.

The figure points out that for each source class, there are a few favorable target classes. These classes contain instances that are geometrically close to the clean source point sets. These instances enable the untargeted attack to craft adversarial examples with *both* low input distortion *and* low output reconstruction error, as Figure 8 examples.

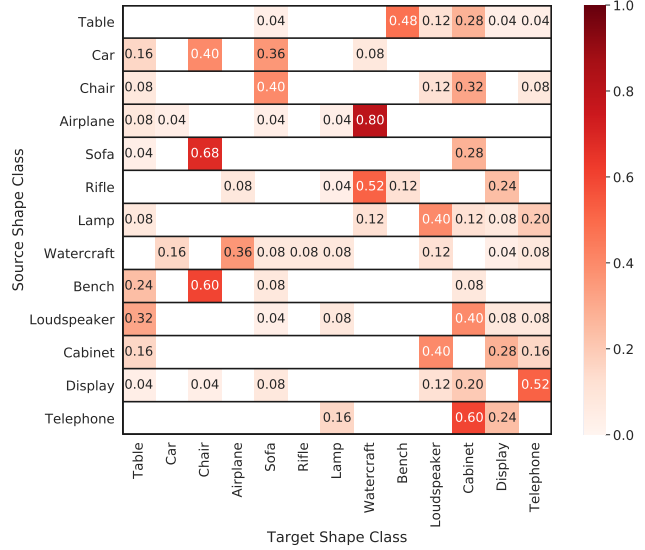


Figure 7. **Untargeted output space attack distribution.** Each row presents the distribution of different target shape classes for the corresponding source shape class. For each source class, the distribution is mostly concentrated at one or two target classes.

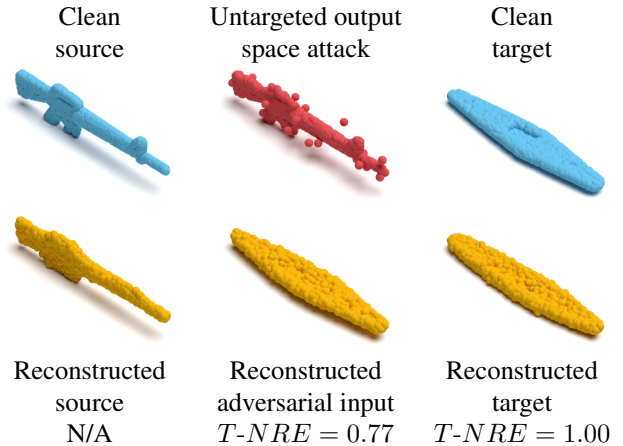


Figure 8. **An untargeted attack example.** Top row: a clean source point cloud (*rifle*), an untargeted attack example, and a clean target (*watercraft*). Bottom row: corresponding reconstructions and their target normalized reconstruction error, $T-NRE$ (not applicable for the reconstructed source). In the untargeted setting, the adversarial perturbation is low, and the reconstruction quality is even better than the reference reconstruction result for a clean target, as indicated by the $T-NRE$ smaller than 1.00.

A.3. Semantic Interpretation

As noted in the paper, the attack may choose target point clouds that are not correctly interpreted semantically. Figure 9 presents the classification confusion matrix for the reconstructions of selected targets of the output space attack. In Figure 10, we show examples of misclassification cases.

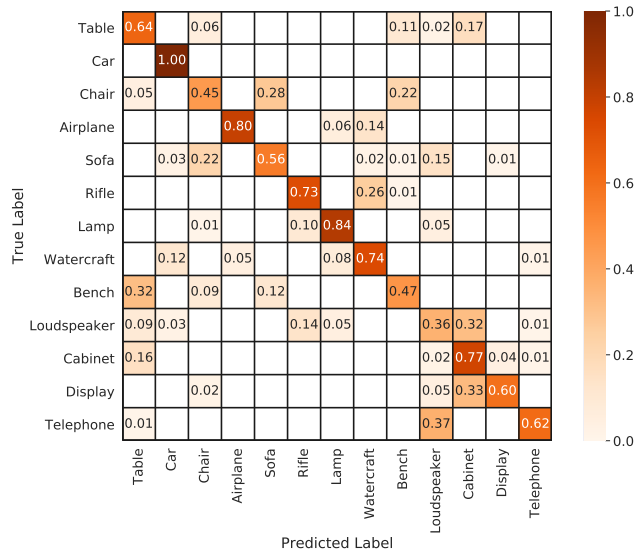


Figure 9. **Confusion matrix for reconstructed clean target point clouds.** Each cell shows the fraction of predicted class label (in the columns) for the corresponding true label (in the rows). Confusion occurs between shape classes that share similar geometric characteristics, such as *chair* and *sofa* classes.

The selection mechanism of a target point set is based on its geometric proximity to the source shape. Thus, the attack may select a non-standard instance from the target class. It leads to confusion modes between shape classes with similar characteristics, such as *sofa* and *chair* or *cabinet* and *table*, as raises from the confusion matrix in Figure 9.

In Figure 10, a tall and narrow *sofa* instance is selected as a target. These features are rare for the *sofa* class, as its shapes are typically shorter or wider (see the sofa examples in Figures 4, 12, and 13). On the other hand, *chair* models in the ShapeNet dataset [4] are usually tall and narrow, and thus, the classifier predicts a *chair* label.

Similar reasoning applies to the unusual target *airplane* shape, which has no wings. This is an example where the reconstructed clean target is labeled as the source’s label - a *watercraft*. We note that for *all* other visual attack examples in the paper and the supplementary material, the reconstructed point cloud is classified as the desired target shape class.

A.4. Failure Cases

Figure 11 presents several failure cases for the output space attack. In such cases, the source point cloud is distorted, and there are points far from the shape’s surface.

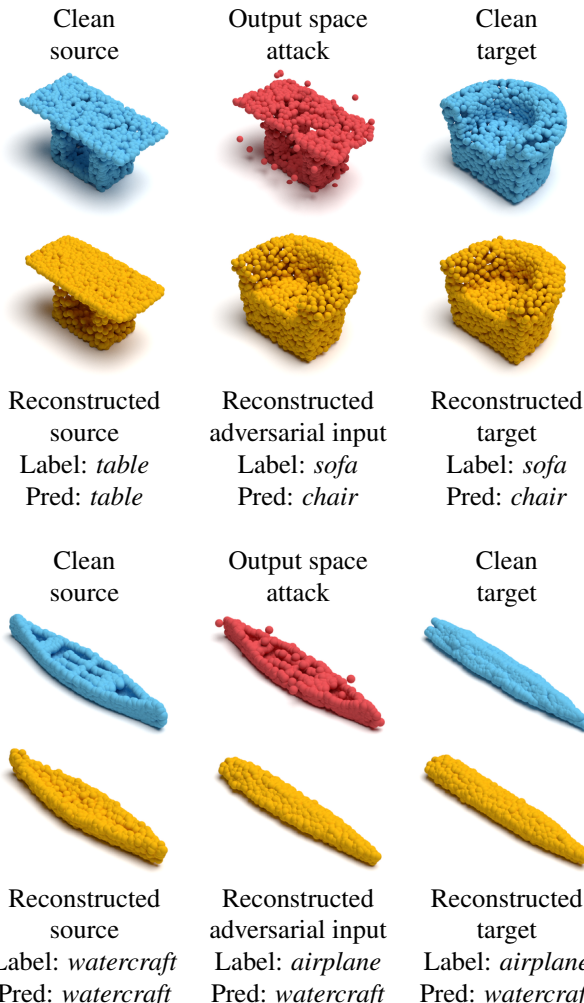


Figure 10. **Target shapes with wrong semantic interpretation.** The first row in each group: a clean source point cloud, an adversarial example, and a clean target. The second row in each group: the corresponding reconstructions. Below the reconstructed point clouds, we indicate their shape class (Label) and predicted label (Pred) by a classifier. Our attack may select targets that are wrongly classified, though the classifier’s mistake is reasonable.

B. Additional Defense Results

B.1. Defense for Untargeted Setting

The paper reports defense results for the *targeted* attack setting (Table 4). Here, in Table 5 and Figure 12, we provide the defense’s results for the *untargeted* case. As explained in sub-section A.2, the untargeted attack causes a mild perturbation to the clean source and results in examples that are easier to defend against. In this case, after removing off-surface or critical points from the adversarial point cloud, the geometry and semantic interpretation of the source are obtained at the AE’s output.

Albeit, there are still light remnants of the attack in the

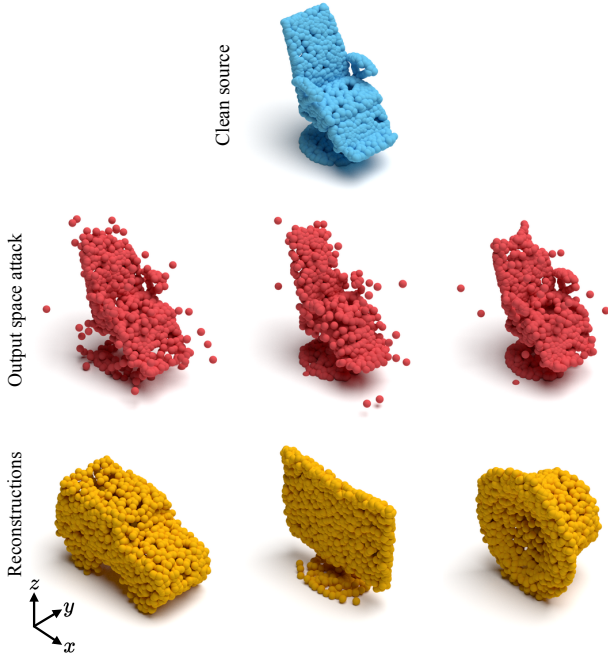


Figure 11. **Failure cases.** Top and middle rows: a clean *chair* and its adversarial examples. Bottom row: corresponding reconstructions of the adversarial examples (a *car*, a *display*, and a *loud-speaker*). The target shape is either too long on the x -axis, thin on the y -axis, or short on the z -axis, compared to the clean source. This geometric discrepancy results in distorted adversarial examples.

reconstruction of the defended point set. For instance, in Figure 12, the output *car* is flatter like the target *sofa*, and the *telephone* becomes shorter as the target *display* shape. We conclude that our attack is not fully defendable, even in the untargeted setting.

B.2. Defense for the Latent Space Attack

In Figure 6 in the paper, we presented a defense example for the output space attack. Here, in Figure 13, we show this example for the latent space attack. Similar to the findings in the paper, the defense does not mitigate the attack’s influence completely. For the latent space attack, the residual effect is even more prominent, as its perturbation of the clean point cloud is stronger than in the output space attack.

B.3. Decoder Side Defense

Our defense is meant to do *attack correction* on the *encoder side*. Meaning, it removes adversarial points from the input to reduce the attack’s effect on the output. However, a residual effect still exists, and features of the attack’s target appear in the reconstructed shape after the defense. On the other hand, the defense has a negligible influence on a clean point cloud, and its reconstruction after applying the

Before/After Off-Surface <i>or</i> Critical Points Defense			
Defense Type	$S-RE \downarrow$	$S-NRE \downarrow$	$S-RCA \uparrow$
Surface (Lat)	4.26/1.25	9.47/2.46	31.4%/79.4%
Critical (Lat)	4.26/ 1.15	9.47/ 2.16	31.4%/ 81.5%
Surface (Out)	4.54/1.02	9.91/1.90	32.0%/85.9%
Critical (Out)	4.54/ 0.94	9.91/ 1.71	32.0%/ 87.4%

Table 5. **Geometric defense metrics and semantics for the untargeted setting.** The acronyms are the same as in Table 4. The $S-RE$ is multiplied by a factor of 10^3 . The arrow indicates whether lower or higher is better. The defenses are successful in reducing the source’s reconstruction error and in increasing its correct classification rate.

Attack \ Defense	Surface	Critical
	Latent	68.0%
Output	59.2%	61.0%

Table 6. **Attack detection accuracy.** The accuracy is for detecting whether a reconstructed point cloud originates from a defended clean or a defended adversarial input. Higher is better. Our attack detector increases the 50% coin-flip accuracy by approximately 20% and 10% for the latent and output space attacks, respectively.

defense remains practically the same.

This state gives rise to another layer of defense - *attack detection* on the *decoder side*. Its goal is to alert whether the reconstructed point cloud came from a tampered input. As proof of concept, we did the following experiment. We split the source-target pairs of our attack into 76%/18%/16% for train/validation/test sets, applied our defense on the clean source and adversarial examples, and ran them through the victim AE. Then, we trained a binary classifier on the reconstructed sets, where the labels for clean and adversarial point clouds were 0 and 1, respectively. The detection accuracy on the test set for our attacks and defenses is given in Table 6.

The baseline accuracy for the detection problem is 50% (a random label choice). Our attack detection mechanism increases this accuracy for both attacks with both defenses. As stated in sub-section B.2, the remaining effect is higher for the latent space attack compared to the output space attack. Thus, the former is easier to detect, and its detection accuracy is almost 70%, where for the latter, it is about 60%. We conclude that attack detection at the decoder side is possible to some extent. Nonetheless, it comes with the overhead of running the defense on the input and the detector on the output constantly.

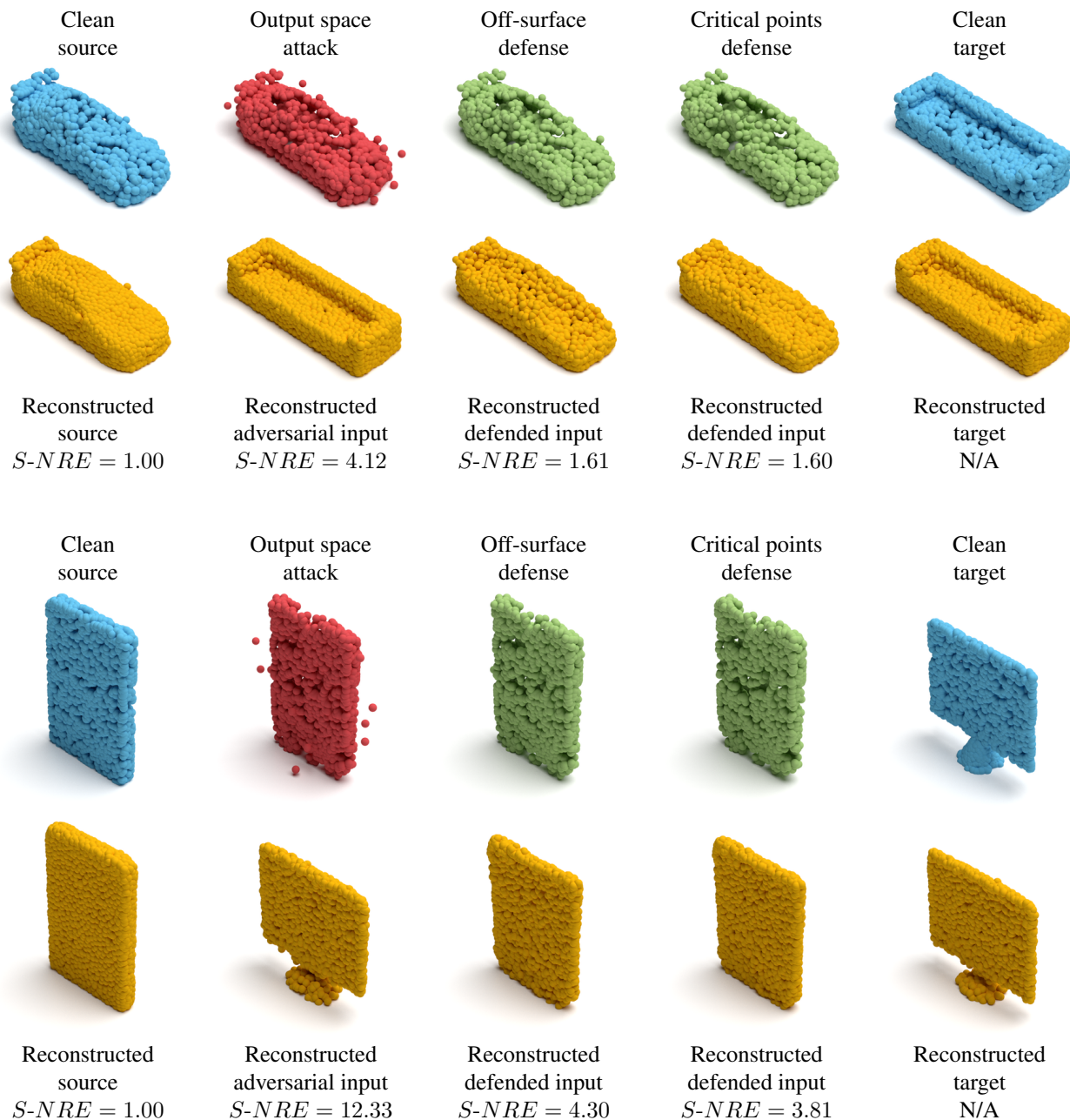


Figure 12. **Defense for untargeted output space attack.** First row: a clean source point cloud (*car*), an adversarial example of the untargeted output space attack, defended point cloud by off-surface defense, defended point cloud by critical points defense, and a clean target (*sofa*). The third row is like the first row, with a *telephone* and a *display* as the source and target shapes, respectively. Second and fourth rows: corresponding reconstructions and their source normalized reconstruction error, $S-NRE$ (not applicable for the reconstructed target). The defenses reduce most of the attack’s effect and return the source shape’s geometry at the output, while a slight residual effect is present in its reconstruction.

C. Ablation Study

C.1. Latent Nearest Neighbors

In the paper, we selected candidates for attack according to the distance in the point space for both the latent and out-

put space attacks (see the last paragraph in Section 3.1). A reasonable alternative for the latent space attack is to choose candidates according to the distance in the latent space. Thus, we ran that attack, where the target for each source was selected from Euclidean nearest neighbors in the latent

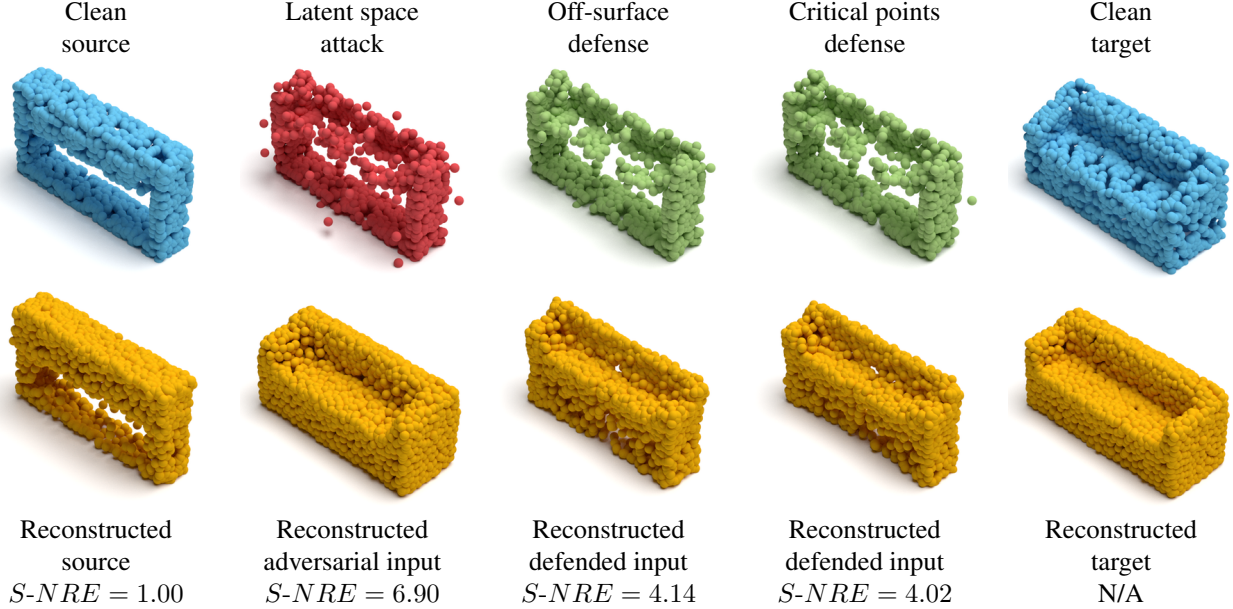


Figure 13. **Defense for the targeted latent space attack.** Top row: a clean source point cloud (*table*), an adversarial example of the targeted latent space attack, defended point cloud by the off-surface defense, defended point cloud by the critical points defense, and a clean target (*sofa*). Bottom row: corresponding reconstructions and their source normalized reconstruction error, $S-NRE$ (not applicable for the reconstructed target). After the defense, remnants of the attack are still much present at the reconstructed output.

space.

The adversarial metric results for this experiment were the same as those reported in Table 1 in the paper. It happened since the proximity *ranking* of geometric nearest neighbors is mostly preserved in the AE’s latent space. Thus, selecting neighbors in the latent space is equivalent to the selection in the point space in terms of the attack’s performance. We decided to use geometric neighbors for both the latent and output space attacks to enable a direct comparison between them.

C.2. Target Selection with Semantic Consideration

Our target selection mechanism is purely geometric. It chooses candidate point cloud instances from the target class according to their Chamfer Distance from the given source point cloud. Then, the point set that yields the lowest attack score (Equation 10) is selected for the corresponding source. As reported in Table 2 in the paper, this results in relatively low classification accuracy for reconstructed targets and adversarial examples.

As an alternative, we restricted the selection to a subset of targets whose reconstruction is recognized correctly by the classifier, which substantially improved the semantic performance. We highlight here that this change influences the attack in several other aspects. First, the classifier becomes part of the method, rather than a means to its evaluation. Now, access to reconstructed point clouds by the victim AE is required. While this assumption is valid for

the output space attack, it was not imposed on the latent space attack before.

Second, it affects the attack’s geometric performance since the classifier rules out potential instances from the target class. Table 7 presents the results for this case. Compared to Table 1, there are additional 2 off-surface (*OS*) points, and the normalized error is higher by 5% (1.14 instead of 1.09). For the latent space attack, it also resulted in 25 *OS* points and a $T-NRE$ of 1.75 instead of 1.65 (a 10% increase).

To conclude, in the paper, we preferred a clear separation between geometric and semantic considerations when performing the attack. However, if a classifier is assumed to be available, it can be beneficial in the semantic aspect to leverage its predictions when selecting target point clouds for the attack, at the expense of some geometric performance reduction.

C.3. Number of Target Candidates

For each source point cloud in our attack, we have 5 candidate instances from the target shape class. As an ablation test, we ran our attack with one target candidate only (the first nearest neighbor). As seen in Table 7, this experiment increased both the source distortion $S-CD$ and target reconstruction error $T-RE$, compared to the results in the paper (Table 1).

We note that in this case, the relative error ($T-NRE$) is 1.02, smaller than that reported in the paper, which was

Attack Results in Ablative Settings				
Attack Type	#OS	S-CD	T-RE	T-NRE
Output (A)	25	0.49	0.63	1.14
Output (B)	25	0.45	0.78	1.02
Output (C)	25	0.45	0.63	1.12
Output (D)	30	0.44	0.67	1.18
Output (E)	25	0.54	0.71	1.27
Output (F)	22	0.41	0.63	1.11

Table 7. **An ablation study for the targeted output space attack.** Geometric adversarial metrics are reported for different variations of our attack (one change at a time): a selection of targets with a correct semantic prediction (A), one target candidate per source (B), one λ value for the distance regularization loss (C), direct perturbation restriction (D), an addition of an off-surface loss (E), and a linear attack score (F). The acronyms are the same as in Table 1 in the paper. The *S-CD* and *T-RE* are multiplied by a factor of 10^3 . Lower is better. The ablative settings either increase the source distortion, compromise the reconstruction quality, or both. See Section C for more details.

1.09. However, the absolute error (*T-RE*) is much higher, and thus, this setting is undesired. To summarize, using several potential targets per source enables the attack to achieve better geometric performance.

C.4. Number of Values for the Distance Loss Weight

The parameter λ in Equations 2 and 6 influences the source distortion and the target reconstruction quality. A small λ value may give good reconstruction quality at the cost of high perturbation of the source. On the contrary, a large value will result in low source distortion and increased target reconstruction error. We tuned λ to balance between the two. As explained in the paper, we optimized the attack with 3 different λ values and selected the value that yielded the minimal attack score (Equation 10) for each source-target pair.

Here, we used only a single value, $\lambda = 1$. As expected, it reduced the attack’s performance (see Table 7). Thus, using several values and selecting the most suitable one for each pair is preferred.

C.5. Direct Perturbation Restriction

In the optimization process of our attack, we employed Chamfer Distance to preserve geometric proximity between the clean source and the adversarial point set. An alternative approach is to restrict the perturbation norm directly by an L_2 loss. In this case, Equation 5 takes the form:

$$\mathcal{L}_{distance}(Q, S) = \|Q - S\|_2 = \|P\|_2. \quad (17)$$

We optimized our attack with the perturbation loss and recalibrated λ to level it with the adversarial loss in Equation 6. The results of this experiment are provided in Table 7. Compared to the adversarial metrics in Table 1, all

the metrics are compromised when the perturbation loss is employed. Similarly, for the latent space attack, using this loss raised the number of *OS* points to 64 and the *T-NRE* to 1.78.

The perturbation loss penalizes perturbed points according to their distance from the original corresponding point in the clean set and does not consider the shape’s geometry. Specifically, it does not account for proximity to other points in the set, as may occur for a shift tangential to the surface. We conclude that direct perturbation restriction hinders the attack’s search space and, therefore, find it less suitable for our purposes.

C.6. Off-Surface Loss

Our distance loss averages the distance between each point in the adversarial example and its nearest neighbor point in the source point set. Thus, the attack may craft an example with mostly on-surface points and several off-surface ones that do not have a close neighbor. In an attempt to minimize the number of off-surface (*OS*) points during the optimization of the attack, we added the maximal nearest neighbor distance to its optimization objective. In this experiment, Equation 5 was changed to:

$$\mathcal{L}_{distance}(Q, S) = CD(Q, S) + \beta \max_{q \in Q} \min_{s \in S} \|q - s\|_2^2, \quad (18)$$

where β is a hyperparameter.

A low value of $\beta = 0.001$ did not influence the number of *OS* points. However, a high β value did not reduce their number but rather increased it and also compromised the reconstruction quality of the attack’s target. For example, setting $\beta = 0.1$ resulted in 25 *OS* points and a *T-NRE* = 1.27 for the output space attack (see Table 7). Similar to direct perturbation restriction (sub-section C.5), the maximal nearest neighbor loss limits the quest of the attack for adversarial solutions with good geometric performance, and thus, we did not use it in our method. This experiment’s result suggests that our attack, as presented in the paper, crafts adversarial examples with both a low number of off-surface points and a low reconstruction error of the target point cloud.

C.7. Linear Attack Score

In the main body, the attack’s score for a source-target pair was the L_2 norm of the source distortion $CD(Q, S)$ and the target reconstruction error $CD(\hat{Q}, T)$ (see Equation 10). As an alternative, we used the sum of these quantities as the score:

$$r = CD(Q, S) + CD(\hat{Q}, T), \quad (19)$$

and evaluated our attack’s geometric performance.

$k \backslash \delta$	0.03	0.04	0.05	0.06
1	4.88	4.88	5.27	5.89
2	5.08	4.82	5.05	5.54
4	5.54	4.98	4.96	5.28
8	6.19	5.41	5.10	5.19

Table 8. **Off-surface defense calibration.** The defense is applied with different parameter settings to the latent space attack. The $S-NRE_{after}$ is computed for each setting. Lower is better. Selecting the number of neighbors $k = 2$ and the distance threshold $\delta = 0.04$ gives the lowest error.

This scoring type yielded very similar results to those reported in Table 1. For the output space attack, it resulted in 22 OS points and a $T-NRE$ of 1.11 (Table 7). We preferred the norm score since it gave a lower reconstruction error, with an increase of only one off-surface point.

C.8. Off-Surface Defense Calibration

The off-surface defense requires the calibration of the number of nearest neighbors k , for computing the average distance per point, and the distance threshold δ . A small k value will result in a noisy distance measure. If k is too large, the average distance will be less discriminative for detecting off-surface points. Regarding the threshold, setting a high value may not filter all the adversarial points, while a small value will filter on-surface points and compromise the reconstruction quality.

We applied the defense for the latent space attack with different k and δ values to obtain a minimal reconstruction error for the defended input, with respect to the clean source point cloud ($S-NRE_{after}$, Equation 14 in the paper). The results appear in Table 8. We found that $k = 2$ gives a discriminative distance measure and $\delta = 0.04$ balances between keeping on-surface points while filtering out-of-surface ones. Thus, this calibration results in the lowest $S-NRE_{after}$. We note that this calibration applies to the output space attack as well.

D. Experimental Settings

D.1. Victim Autoencoder

We adopt the published AE architecture of Achlioptas *et al.* [1]. The encoder has 5 per-point convolution layers, with filter sizes (64, 128, 128, 256, m). Each layer includes batch normalization and ReLU operations. The last layer is followed by a global feature-wise max-pooling operation to obtain a latent feature-vector of size $m = 128$. The decoder is a series of 3 fully-connected layers, with sizes (256, 256, $n \times 3$), where $n = 2048$ is the number of output points. The first two layers of the decoder include ReLU non-linearity. We train the AE with Chamfer Distance loss

	MLP [1]	AtlasNet [11]	FoldingNet [42]
TEs	500	150	25
BS	50	32	8
LR	0.0005	0.001	0.0001
TT	6	7	153

Table 9. **Training settings of the attacked AE and the AEs for transfer.** MLP refers to the attacked AE. AtlasNet and FoldingNet are the AEs for transfer. TEs, BS, LR, and TT stand for training epochs, batch size, learning rate, and training time, respectively. The training time is reported in hours for an Nvidia Titan Xp GPU.

Parameter	Value
Gradient steps	500
Learning rate	0.01
$\{\lambda\}$ Perturbation/Latent	{0.075, 0.1, 0.125}
$\{\lambda\}$ Perturbation/Output	{0.0005, 0.001, 0.003}
$\{\lambda\}$ Chamfer/Latent	{50, 100, 150}
$\{\lambda\}$ Chamfer/Output	{0.5, 1, 5}

Table 10. **Optimization parameters.** The table details parameter values for our attacks. We indicate the λ parameter for different distance/adversarial loss type settings. Perturbation and Chamfer refer to Equations 17 and 5, respectively. Latent and Output refer to Equations 3 and 7, respectively.

(Equation 4 in the paper) and Adam optimizer with momentum 0.9, as recommended by the authors. Additional settings appear in Table 9.

D.2. Attack Optimization

Table 10 summarizes the optimization parameters for our attacks. We ran the optimization for 500 gradient steps. Starting from iteration 400, near the convergence point of the attack, we checked the target reconstruction error and kept the result with the minimal error. On average, the optimization time for a single input point cloud was 0.69 seconds for the latent space attack and 0.72 seconds for the output space attack.

D.3. Autoencoders for Attack Transfer

We trained an AE with the same architecture as the attacked one, as detailed in sub-section D.1. The training settings were also the same, up to a different random weight initialization. For the other AEs for the transfer experiment, we followed the official implementation [11] or published paper [42] of the authors.

AtlasNet [11] employs a PointNet-based encoder. It has a multi-layer perceptron (MLP) of size (64, 128, 1024), followed by a global max-pooling over points and fully-connected layers of sizes (1024, 1024). Each encoder layer has batch normalization and ReLU activation, except the last MLP layer that is without batch normalization. The en-

coder produces a global latent vector of size 1024.

The decoder operates on sets of 2D points from the unit square. First, it applies a per-point filter of size 1024 and adds the global latent vector to each point. Then, it uses an MLP of size (512, 512, 512, 3) to obtain the output 3D point cloud. All the layers include batch normalization and ReLU, except for the last layer. The decoder runs on 25 2D unit squares, with 100 points at each square, and outputs 2500 points in total.

FoldingNet [42] takes as input xyz coordinates and the local covariance for each point. Its encoder contains an MLP of 3 layers, with filter sizes (64, 64, 64). Then, two graph layers aggregate information from 16 neighboring points and increase the number of point features to 1024, with an MLP of size (128, 1024). A global max-pooling and additional 2 fully-connected layers of sizes (512, 512) produce a 512-dimensional latent code-word. Each layer of the encoder, except the last one, includes batch normalization and ReLU activation.

The decoder concatenates the code-word to 2D grid points and folds them two times to reconstruct the 3D shape. Each fold is implemented by an MLP of size (512, 512, 3), with ReLU non-linearity in the first two layers of the MLP. The 2D grid contains 2025 points, which is the number of 3D output points.

We trained the AEs with Chamfer Distance loss (Equation 4), as employed for the victim AE. Additional training settings are given in Table 9.

D.4. Classifier for Semantic Evaluation

We used PointNet architecture with 13 output classes, the number of shape classes for our attack. We trained the network with the same settings as Qi *et al.* [29], with 140 epochs instead of 250 and without random point cloud rotation during training. These modifications improved the classification performance in our case. Training the classifier took about 17 hours.

D.5. Classifier for Decoder Side Defense

The classifier for this experiment (sub-section B.3) was a PointNet with 2 output labels. We used the same training settings as Qi *et al.* [29], except for random rotation during training and a different number of epochs. For the latent and output space attacks, with both defenses, we trained the classifier for 80 and 100 epochs, respectively. The training took approximately 1 and 1.25 hours for the corresponding classifier instance.



Figure 14. **Attack evolution.** Top three rows: interpolation between a clean source point cloud (a *bench*, leftmost at the first row) and an adversarial example (targeted to a *car*, rightmost at the third row). Bottom three rows: corresponding reconstructions. The interpolation weight α from left to right is: $\{0.0, 0.05, 0.1, 0.2, 0.25\}$ (first row), $\{0.3, 0.4, 0.5, 0.6, 0.7\}$ (second row), and $\{0.75, 0.8, 0.9, 0.95, 1.0\}$ (third row). The adversarial point set evolves such that its reconstructions transition smoothly from the source to the target shape.